Original Paper

phys. stat. sol. (b) **244**, No. 6, 2233–2241 (2007) / **DOI** 10.1002/pssb.200642028

Magnetic ordering of Mn and Ru in $(La_{0.52}Ba_{0.48})(Mn_{0.51}Ru_{0.49})O_3$

S. Y. Wu[*, 1], **W.-H. Li**[2], **C. C. Yang**[2], **J. W. Lynn**[3], and **R. S. Liu**[4]

[1] Department of Physics, National Dong Hwa University, Hualien 97401, Taiwan
[2] Department of Physics, National Central University, ChungLi 32054, Taiwan
[3] NIST Center for Neutron Research, NIST, Gaithersburg, MD 20899-8562, USA
[4] Department of Chemistry, National Taiwan University, Taipei 106, Taiwan

Received 19 January 2006, revised 16 January 2007, accepted 14 February 2007
Published online 26 March 2007

PACS 61.12.Ld, 75.25.+z, 75.47.Gk

Neutron diffraction, dc magnetization, and ac magnetic susceptibility measurements have been performed to study the magnetic properties of perovskite $(La_{0.52}Ba_{0.48})(Mn_{0.51}Ru_{0.49})O_3$. The compound crystallizes into a cubic $Pm\bar{3}m$ symmetry with a lattice constant of $a = 3.9661(4)$ Å at room temperature. Two anomalies, at around 160 and 60 K, can clearly be seen in the ac susceptibility results, with the peak positions for both anomalies shifting to a higher temperature as a dc magnetic field is applied. Neutron magnetic diffraction measurements show that the anomalies that occur at high and low temperatures are associated with the ferromagnetic ordering of the Mn and the Ru spins, respectively. The ordering temperatures for the Mn and Ru spins were found to be T_C (Mn) ≈ 195 K and T_C (Ru) ≈ 80 K, with a saturated moment of $\langle\mu_{z\text{-Mn}}\rangle = 2.21(5)\mu_B$ for the Mn spins and $\langle\mu_{z\text{-Ru}}\rangle = 1.00(5)\mu_B$ for the Ru spins.

1 Introduction

The transport and magnetic properties of general formula $(La_{1-x}A_x)(Mn_{1-y}B_y)O_3$ manganite perovskite, where A is an alkaline-earth metal and B a transition metal, are known to be sensitive to both A-site and B-site doping [1–5]. Generally speaking, A-site doping creates a Mn^{3+}/Mn^{4+} mixed-valence state that not only affects the carrier density but also significantly influences the colossal magnetoresistance exhibited by this class of material [6]. These A-site doping systems exhibit a surprising wide variety of magnetic and structural phases, such as metallic ferromagnetic $La_{0.7}Ba_{0.3}MnO_3$ with higher Curie temperature T_C ~350 K [7], lattice effects in doped $LaMnO_3$ that tuned the Curie temperature adjusted by varying the A-site doping [8, 9], structurally changing from well known Pnma to Imma for larger ionic radius of the A-site $\langle r_a\rangle$ [10], and magnetic phase transition from single phase ferromagnetic metallic state to multi-phase ferromagnetic insulating state at x near 0.5 [11]. Recently, A-site ordered $La_{0.7}Ba_{0.3}MnO_3$ has been synthesized by Millange et al. [12], where LaO and BaO planes alternately stack along the c-axis to form a P4/mmm structure, which reveals different physical properties from the common cubic $Pm\bar{3}m$ symmetry. The doping of Mn sites in $(La_{1-x}A_x)(Mn_{1-y}B_y)O_3$ systems with ruthenium means that charges are transported through the Mn–O–Mn network via double-exchange interactions [13]. Recently, studies on a similar interesting system, $Tl_2Mn_{2-x}Ru_xO_7$ compound [14, 15], have shown the Ru^{4+} substitution in the Mn^{4+} networks, resulting in a magnetoresistance increase as the charge density in the Tl–O conduction band is reduced. Goodenough [16] pointed out that ferromagnetism is governed not only by the double exchange reactions, but also by the nature of the superexchange interactions. The electronic configuration of Ru should allow ferromagnetic superexchange interactions with Mn^{3+} [17]. Such Ru induced

[*] Corresponding author: e-mail: sywu@mail.ndhu.edu.tw, Phone: +88 63 863 371 7, Fax: +88 63 863 369 0

ferromagnetism in the Mn^{4+} rich manganites has also been reported by B. Raveau [18] and C. Martin [19, 20]. B-site doping, on the other hand, disrupts the electrically and magnetically active Mn–O–Mn network, weakening the DE interaction, and is believed to be detrimental to the conduction mechanism. A significant reduction in the Curie temperature due to Al, Fe, and Ti doping onto the B-sites has been reported [21], indicating that both the electrical and magnetic properties can be strongly affected by B-site doping. In this paper, we report on the crystalline structure and magnetic ordering of Mn and Ru in 50% A-site and 50% B-site doped $(La_{0.5}Ba_{0.5})(Mn_{0.5}Ru_{0.5})O_3$, studied by using dc magnetization, ac magnetic susceptibility, and neutron diffraction measurements.

2 Experimental details

A 50% A-site and 50% B-site doped polycrystalline sample with a nominal composition of $(La_{0.52}Ba_{0.48})(Mn_{0.51}Ru_{0.49})O_3$ was prepared from high-purity $BaCO_3$, La_2O_3, Mn_2O_3, and RuO_2 powders by employing the standard solid-state reaction technique [19, 22]. Mixtures of these powders were pressed into pellets and prepared by heating at a sintering temperature of 1350 °C for 24 h. The regrinding, pressing, and sintering process was repeated three times. X-ray diffraction was first used to characterize the sample, pellet by pellet. No obvious differences were found in the X-ray diffraction patterns taken from different portions of the sample.

3 Results and discussion

3.1 High-resolution neutron powder diffraction

High-resolution neutron powder-diffraction was then employed to determine the detailed crystalline structure. The measurements were performed at the NIST Center for Neutron Research and the data were collected on BT-1, the 32-detector powder diffractometer, using a Cu(311) monochromator crystal to extract neutrons of wavelength 1.5402 Å. Angular collimators, with horizontal divergences of 15′, 20′, and 7′ full width at half maximum (FWHM) acceptance, were employed for the in-pile, monochromatic, and diffracted beams, respectively. During the measurement the sample was loaded into a cylindrical vanadium-can, which gives rise to no measurable neutron diffraction peaks.

The diffraction patterns were analyzed using the General Structure Analysis System (GSAS) program, [23] following the Rietveld refinement method [24]. Several models with different symmetries were assumed during the preliminary analysis. In our structural analysis we then pay special attention to searching for the possible symmetries that can describe the observed diffraction pattern well. All the structural and lattice parameters were allowed to vary simultaneously, and refining processes were carried out until R_p, the weighted R_{wp} factor, differed by less than one part in a thousand within two successive cycles.

One of the concerns about the structure of $(La_{0.5}A_{0.5})(Mn_{0.5}B_{0.5})O_3$ is that whether the B-sites are atomically ordered to provoke Mn–O–B interactions. The ordering is generally favourable if the ionic sizes of the atoms on B are largely different, as has been observed in Ba_2FeRuO_6 and Sr_2FeMoO_6 [25, 26]. In addition, doping onto the A-sites may create distortions due to the appearance of two different atoms in separating the $(Mn/Ru)O_6$ octahedrons. In our structural analysis we then pay special attention to searching for lattice distortion, occupancy factor, and atomic ordering of the Mn/Ru atoms. No atomic orderings of the A or B sites were found. These results are similar to what has been found in separate studies [21, 27]. The refinement was finally carried out assuming a cubic $Pm\bar{3}m$ symmetry, with (Mn/Ru) located at the corners, (La/Ba) occupies the center of the cube, and O located between the (Mn/Ru) atoms, as shown in the inset to Fig. 1. Figure 1 shows the diffraction pattern taken at room temperature, where the solid curves indicate the fitted pattern and the differences between the observed and the fitted patterns are plotted at the bottom of Fig. 1. Careful analysis of the occupancy factors gave a chemical composition of $(La_{0.52}Ba_{0.48})(Mn_{0.51}Ru_{0.49})O_3$ for the compound, which agrees very well with the stoichiometric compound. The occupancy factor of oxygen atom was also refined in the final run

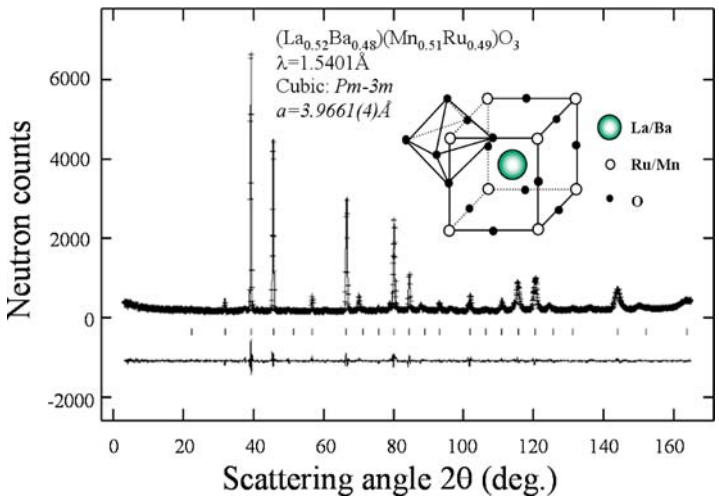

Fig. 1 (online colour at: www.pss-b.com) Observed (crosses) and the fitted (solid curves) diffraction patterns obtained at room temperature. The calculation was based on assuming a space group of $Pm\bar{3}m$ symmetry, as shown in the inset.

and full occupancy was obtained. Good agreement factors $R_p(\%) = 4.37$, $R_{wp}(\%) = 5.64$, and $\chi^2 = 1.627$ were reached. The formation of a cubic $Pm\bar{3}m$ symmetry, with the Mn and Ru ions on the octahedral sites randomly distributed, for the present 50% Ba and 50% Ru doped compound is confirmed, indicating that the ionic radii of Mn and Ru are not significantly different and that the La/Ba atoms are large enough to stabilize a cubic structure. Details of the refined structural parameters are listed in Table 1.

3.2 AC susceptibility

The magnetic properties of the system were first studied by measuring the ac magnetic susceptibility and dc magnetization, using the conventional Quantum Design physical property measurement system set-ups. For the ac susceptibility, both the in-phase component $\chi'(T)$ and the out-of-phase component $\chi''(T)$ were measured, covering from 1.4 to 300 K. These data were collected by employing weak driving fields with various strengths and frequencies, with and without the presence of an applied dc magnetic field. We note that $\chi'(T)$ measures the response of the system to the driving field, whereas $\chi''(T)$ signifies the dissipative loss of the driving field to the system. Figures 2(a) and (b) present the $\chi'(T)$ (filled symbols) together with $\chi''(T)$ (open symbols) at $H_a = 0$ and 1 kOe, respectively. Two anomalies are evident in

Table 1 Refined structural parameters of $(La_{0.52}Ba_{0.48})$ $(Mn_{0.51}Ru_{0.49})O_3$ at room temperature. *B* represents the isotropic temperature parameter.

$(La_{0.52}Ba_{0.48})$ $(Mn_{0.51}Ru_{0.49})O_3$, room temperature, space group: cubic $Pm\bar{3}m$, a = 3.9661(4) Å					
atom	*x*	*y*	*z*	*B* (Å^2)	occupancy
La	0.5	0.5	0.5	0.97(3)	0.52
Ba	0.5	0.5	0.5	0.97(3)	0.48
Mn	0	0	0	1.83(4)	0.51
Ru	0	0	0	1.83(4)	0.49
O	0.5	0	0	1.94(2)	1
		$R_p(\%) = 4.37\%$	$R_{wp}(\%) = 5.64\%$	$\chi^2 = 1.627$	

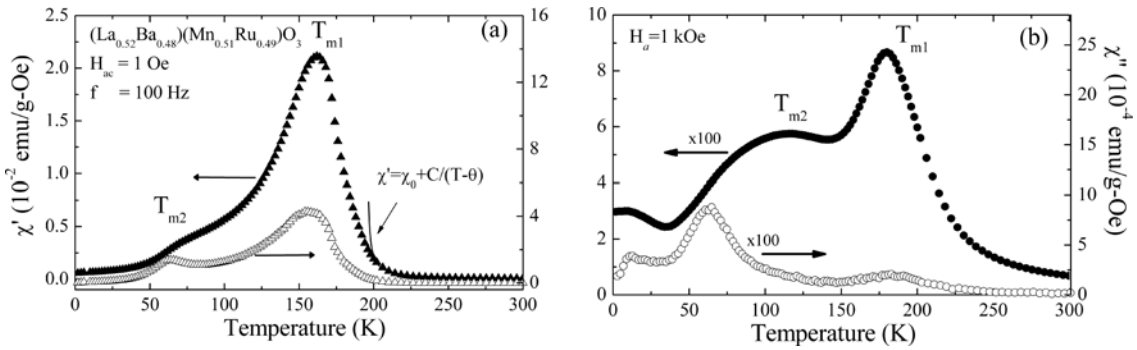

Fig. 2 Temperature dependencies of $\chi'(T)$ (filled symbols) and $\chi''(T)$ (open symbols) with applied magnetic fields of (a) $H_a = 0$ and (b) $H_a = 1$ kOe. Two anomalies marked as T_{m1} and T_{m2} are clearly evident. The solid line shown in Fig. 2(a) is a fit of the data obtained between $190 < T < 300$ K to the Curie–Weiss expression.

$\chi'(T)$, marked as T_{m1} and T_{m2}. Each anomaly is associated with a dissipative loss, as seen in $\chi''(T)$. The anomalies at T_{m1} and T_{m2} originated from the ordering of the Mn and Ru moments, respectively. The peak positions of both anomalies shift to higher temperatures when an H_a is applied, signalling the ferromagnetic character of both the Mn and the Ru moments. The high-temperature portion of $\chi'(T)$ displays a Curie–Weiss ferromagnetic coupling behaviour. The solid curve shown in the high temperature portion of Fig. 2(a) is an extrapolation of the fit of the data obtained between 190 and 300 K to the expression $\chi' = \chi + C/(T - T_\theta)$, where C and T_θ are the Curie–Weiss constant and Curie–Weiss temperature, respectively, and where the temperature independent term χ represents the paramagnetic contribution from the conduction electrons. The fitting results give $T_\theta = 195$ K for the Curie–Weiss temperature and $\mu_{eff} = 4.00(5)\mu_B$ for the effective moment. The positive value of T_θ obtained from the fit, indicates that the ferromagnetic character of the Mn spins agrees with the magnetic neutron diffraction results (see below). The calculation of the effective moment using the fitted value for C is only 5% smaller than the value of $4.2\mu_B$ expected for the free Mn^{3+} ions [27] and larger than that observed for the other double perovskite compound of $La_{0.5}Ba_{0.5}MnO_3$ [29].

In Figs. 3(a) and (b), we show the effects of the strength of the driving field and frequency on $\chi'(T)$ at $T = 1.8$ K, respectively. The value of $\chi'(T)$ goes higher when higher driving field was used (Fig. 3(a)). As the strength of the driving field was raised, the susceptibility responses increased slower with increasing driving field, and thus a field strength of several Oe is not strong enough to alter Mn/Ru spins. The Mn/Ru spins respond "better" to lower frequencies (Fig. 3(b)). This frequency-dependent behaviour becomes less pronounced in the higher frequency regime, indicating the relaxation rate of the magnetic spins is relatively slow and insignificant for spin glass characteristics.

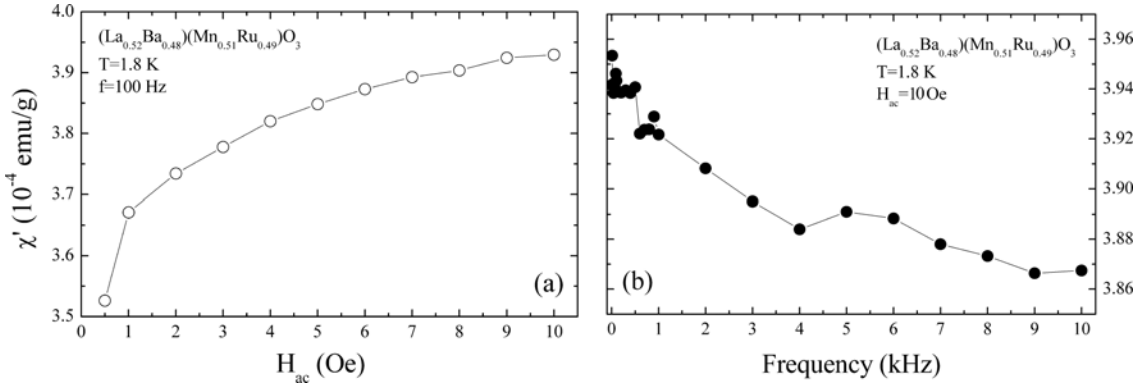

Fig. 3 Effects of the strength of driving field and frequency on χ' at $T = 1.8$ K.

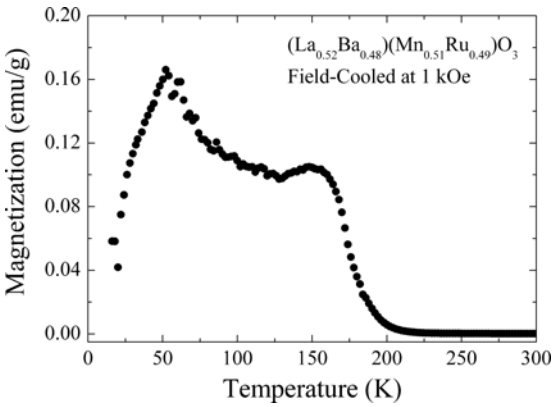

Fig. 4 Temperature dependence of the magnetization measured after field-cooling at 1 kOe. Two distinct peaks are clearly seen, and the magnetization decreases rapidly below 50 K.

The two anomalies observed in $\chi'(T)$ are also evident in the magnetization curve, shown in Fig. 4. These data were collected in a warming cycle, after being field-cooled at 1 kOe to the lowest temperature obtained. Rapid increases in magnetization are seen below ~200 and ~90 K, while a plateau appears between these two temperature regimes, which show that the two anomalies are associated with two separate magnetic phases.

3.3 Isothermal magnetization

The field dependence of the magnetization in Bohr magnetons per formula unit of $(La_{0.52}Ba_{0.48})(Mn_{0.51}Ru_{0.49})O_3$ at 2 K is shown in Fig. 5. At low H_a the magnetization increases rapidly with increasing H_a, reflecting the existence of ferromagnetic spin correlations. A difference of the magnetization history like this behaviour is due to the relaxation process for magnetization, since the B-sites are randomly arranged from the results of their structural parameters. The other characteristic of the results is that the initial magnetization is out of the M–H loop, which is the same as in previous reports [25]. The inset to Fig. 5 shows the variations of the magnetization with the applied magnetic field, $M(H_a)$, taken at several temperatures. No noticeably differences in the magnetization curves were found between the measurements made with a field-increasing loop and a field-decreasing loop. There are apparently two magnetic components that were observed: a paramagnetic component that can be aligned by H_a above T_c, and a ferromagnetic one that becomes dominating at high H_a below T_c. The saturated magnetic moments obtained at T = 100 K and 2 K were ~1 and 1.3μ_B, respectively.

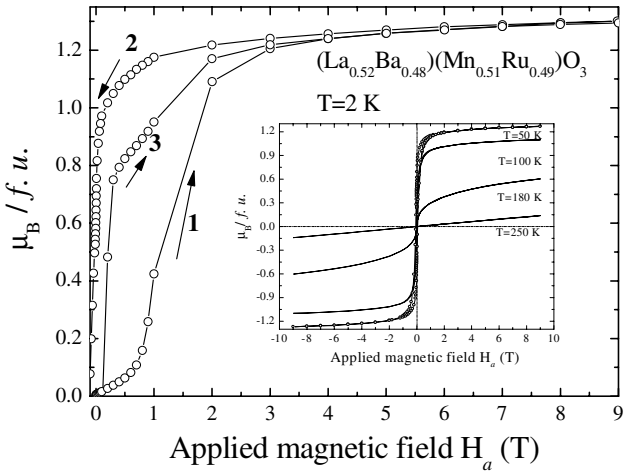

Fig. 5 Magnetization in Bohr magnetons per formula unit of the $(La_{0.52}Ba_{0.48})(Mn_{0.51}Ru_{0.49})O_3$ sample, measured at several temperatures.

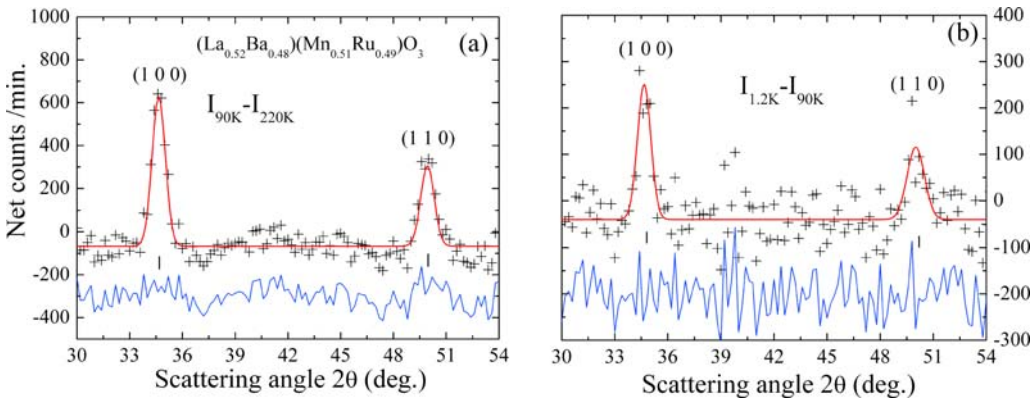

Fig. 6 (online colour at: www.pss-b.com) Magnetic peaks develop as the temperature is reduced from (a) 220 to 90 K and (b) from 90 to 1.2 K. The solid lines are the fitted pattern, using the Rietveld method. Shown at the bottom are the differences between the observed and the fitted patterns.

3.4 Magnetic neutron diffraction

Neutron magnetic diffraction patterns, covering certain temperature regimes where the susceptibility shows anomalies were collected to search for magnetic signals. These measurements were also conducted at the NIST Center for Neutron Research, using a BT-9 triple-axis spectrometer and a pyrolytic graphite PG (002) monochromator crystal to extract $\lambda = 2.359$ Å neutrons, with a PG filter to suppress higher-order wavelength contamination. Angular collimations with horizontal divergences of 40′, 48′, and 48′ FWHM acceptance were used for the in-pile, monochromatic, and diffracted beams, respectively. The sample was mounted in a cylindrical vanadium can filled with helium exchange gas to facilitate thermal conduction, and a pumped ^{4}He cryostat was used to cool the sample. Diffraction patterns, covering the angular range from $2\theta = 5°$ to 65°, were collected at several temperatures. No significant structural changes were observed over the temperature range studied.

In Figs. 6(a) and (b) we show the portions of the magnetic diffraction patterns obtained at 90 K and 1.2 K, where the diffraction patterns taken at 220 and 90 K, which serve as the background, have been subtracted from the data to isolate the magnetic signal. The indices shown are based on the low temperature nuclear cubic $Pm\bar{3}m$ unit cell. Shown at the bottom of Figs. 6(a) and (b) are the differences between the observed and the fitted patterns, using Rietveld method [24]. Only nuclear peaks were seen in the pattern taken at 220 K (not shown). As the temperature was reduced to 90 K, the intensities of both reflections, shown in Fig. 6(a) increased significantly. The magnetic diffraction patterns that are associated with the developments of the Mn and the Ru moments are shown in Figs. 6(a) and (b).

3.5 Magnetic spin structure

A ferromagnetic arrangement as shown in Fig. 7(a), where the Mn moments lie along the crystallographic axis direction with a saturated moment of $\langle\mu_{z\text{-Mn}}\rangle = 2.21(5)\mu_B$, fits the pattern observed at 90 K well. For clarity of presentation, the spin direction is chosen to point along the *c*-axis, since our powder neutron data cannot resolve between the three axes, due to their similarity. Figure 6(b) shows that the difference magnetic pattern of 1.2 K reveals two peaks that appeared at the same scattering angles as the nuclear ones do, indicating a ferromagnetic arrangement of the ordered Ru moments. A ferromagnetic arrangement, where the moment points in a direction that is 46° away from the *c*-axis and 78° from *a*-axis within the *a*–*b* plane, as is shown in Fig. 7(b), fits the observed pattern well by using the Rietveld refinement method [24]. The saturated moment obtained for the Ru spins is $\langle\mu_{z\text{-Ru}}\rangle = 1.00(5)\mu_B$. The solid curves shown in Fig. 6 indicate the fits of the data using the Rietveld method, showing that the proposed model describes the observed data well. However, work on single-crystal samples, where more

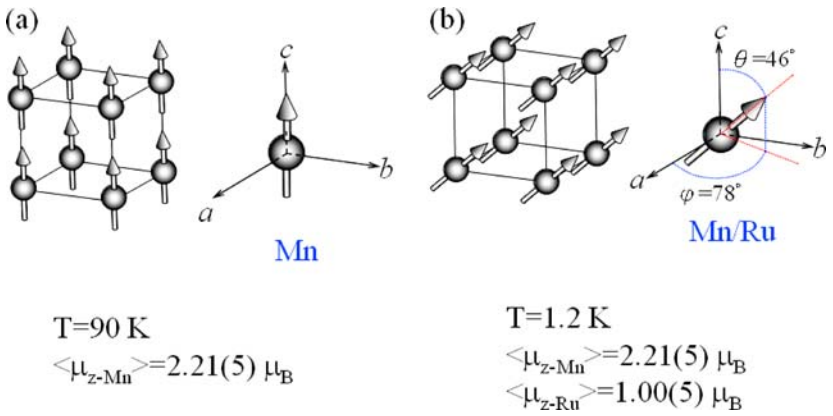

Fig. 7 (online colour at: www.pss-b.com) Proposed spin configurations of the Mn and Ru ions in $(La_{0.52}Ba_{0.48})(Mn_{0.51}Ru_{0.49})O_3$.

magnetic reflections may be identified, will be needed to elucidate the detailed arrangement for the Ru and Mn spins. Compared with the isothermal magnetization results (see Section 3.3), the total ordered moments take the form of $\langle\mu_{z\text{–Mn/Ru}}\rangle = \langle\mu_{z\text{–Mn}}\rangle \times 51\% + \langle\mu_{z\text{–Ru}}\rangle \times 49\%$. A at 90 and 1.2 K they are 1.12 and $1.62\mu_B$, respectively. A good agreement is observed between both results with only slight differences, indicating the existence of inter-grain interaction in the sample.

3.6 Order parameters

On reducing temperature, the intensities of both the {100} and {110} reflections increase accordingly, signaling the development of ferromagnetic moments. Figure 8 shows the temperature dependencies of the {100} and {110} peak intensities, which represent the variation of the square of the order parameter with temperature. A two-step transition is seen in the scattering for the {100} and {110} peak positions, which contains contributions from both magnetic components. The two peaks follow essentially the same temperature dependent curve, showing that they are the two components from the same origin. Accordingly, the ferromagnetic moments begin to develop below 200 K, which originates from the ordering of the Mn moments. It reaches a plateau at around 100 K, as seen in the inset to Fig. 8, showing that the Mn moments have saturated. The ordering temperatures of the Mn spins, as determined by the inflection point of the order parameter curve, are T_C (Mn) ≈ 195 K, which match the temperature at which

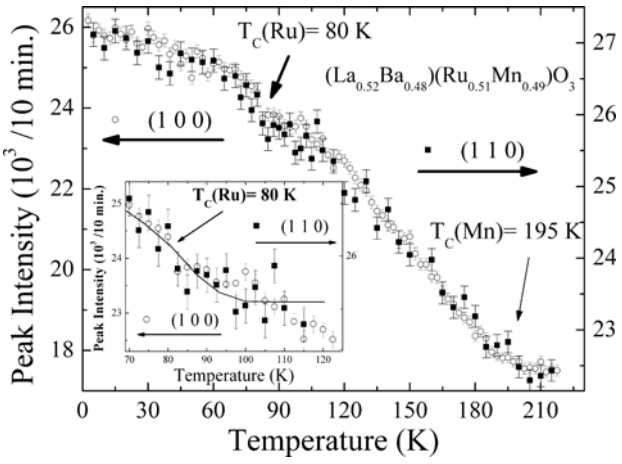

Fig. 8 Temperature dependencies of the {100} and {110} peak intensities, showing that T_C (Mn) ≈ 195 K and T_C (Ru) ≈ 80 K. A portion of Fig. 8 is shown in the inset, where the solid curve is a guide to the eyes only.

$\chi'(T)$ shows an anomaly. The ordering temperature found for the Mn spins in the compound is higher than the temperature at which the Mn spin ordering in $La_{0.5}Ba_{0.5}MnO_3$ results [29]. A second increase in the order parameter is seen below 80 K, revealing the development of the Ru moments with an ordering temperature of $T_C(\mathrm{Ru}) \approx 80$ K.

4 Summary

We have studied the crystal structure and magnetic properties of a polycrystalline $(La_{0.52}Ba_{0.48})(Mn_{0.51}Ru_{0.49})O_3$ sample, fabricated using the standard solid state reaction techniques. The compound of perovskite $(La_{0.52}Ba_{0.48})(Mn_{0.51}Ru_{0.49})O_3$ crystallized into a cubic $Pm\bar{3}m$ symmetry. Two anomalous transitions, at around 160 and 60 K, were clearly observed in the ac susceptibility to be associated with Mn spin ordering and Ru spin ordering. As a dc magnetic field is applied, the peak positions for both anomalies shift to higher temperatures, revealing a ferromagnetic character for both the Mn and Ru moments. Neutron magnetic diffraction measurements then show that the anomalies at high and low temperatures were determined at $T_C(\mathrm{Mn}) \approx 195$ K and $T_C(\mathrm{Ru}) \approx 80$ K from the results of temperature dependent peak intensities, being associated, respectively, with the ferromagnetic ordering of the Mn and the Ru spins which point in the *c*-axis direction and a canted angle off the *c*-axis, respectively, resulting in a ferromagnetic structure at low temperature.

Acknowledgements We thank the financial support of the National Science Council of the Republic of China to the projects NSC 95-2112-M-259-012(NDHU) and NSC 94-2120-M-008-MY3(NCU), and we are grateful to NIST for making all neutron diffraction facilities available.

References

[1] C. N. R. Rao and B. Raveau, Colossal Magnetoresistance, Charge Ordering and Related Properties of Magnetic Oxides (World Scientific, Singapore, 1998).
[2] Y. Tokura, Colossal Magnetoresistance Oxides (Gordon & Breach, London, 1999).
[3] I. Fernandez, R. Greatrex, and N. N. Greenwood, J. Solid State Chem. **32**, 97 (1980).
[4] Manh-Huong Phan, The-Long Phan, Seong-Cho Yu, Nguyen Duc Tho, and Nguyen Chau, phys. stat. sol. (b) **241**, 1744 (2004).
[5] Zhi-Qi Kou, Xiao Ma, Nai-Li Di, Qing-An Li, and Zhao-Hua Cheng, phys. stat. sol. (b) **242**, 2930 (2005).
[6] S. Jin, T. H. Tiefel, M. McCormack, R. A. Fastnacht, R. Ramesh, and L. H. Chen, Science **264**, 413 (1994).
[7] Tapan Chatterji, L. P. Regnault, and W. Schmidt, Phys. Rev. B **66**, 214408 (2002).
[8] H. Y. Hwang, S.-W. Cheong, P. G. Radaelli, M. Marezio, and B. Batlogg, Phys. Rev. Lett. **75**, 914 (1995).
[9] E. O. Wollan and W. C. Koehler, Phys. Rev. **100**, 545 (1955).
[10] P. G. Radaelli, M. Marezio, H. Y. Hwang, and S.-W. Cheong, J. Solid State Chem. **122**, 444 (1996).
[11] H. L. Ju, Y. S. Nam, J. E. Lee, and H. S. Shin, J. Magn. Magn. Mater. **219**, 1 (2000).
[12] F. Millange, V. Caignaert, B. Domenges, B. Raveau, and E. Suard, Chem. Mater. **10**, 1974 (1998).
[13] P.-G. de Gennes, Phys. Rev. **118**, 141 (1960).
[14] Y. Shimakawa, Y. Kubo, and T. Manako, Nature (London) **379**, 53 (1996).
[15] B. Martinez, R. Senis, J. Fontcuberta, and X. Obradors, Phys. Rev. Lett. **83**, 2022 (1999).
[16] J. B. Goodenough, Prog. Solid State Chem. **122**, 444 (1996).
[17] A. Callaghan, C. W. Moeller, and R. Ward, Inorg. Chem. **5**, 1572 (1966).
[18] B. Raveau, A. Maignan, C. Martin, R. Mahendiran, and M. Hervieu, J. Solid State Chem. **151**, 330 (2000).
[19] C. Martin, A. Maignan, M. Hervieu, B. Raveau, and J. Hejtmanek, Eur. Phys. J. B **16**, 469 (2000).
[20] A. I. Shames, E. Rozenberg, C. Martin, A. Maignan, B. Raveau, G. Andre, and G. Gorodestsky, Phys. Rev. B **70**, 134433 (2004).
[21] K. Ramesha, V. Thangadurai, D. Sutar, S. V. Aubramanyam, G. N. Subbanna, and J. Gopalakrishnan, Mater. Res. Bull. **35**, 559 (2000).
[22] B. Raveau, A. Maignan, C. Martin, and M. Hervieu, Mater. Res. Bull. **35**, 1579 (2000).
[23] A. C. Larson and R. B. Von Dreele, General Structure Analysis System, Report LA-UR-86-748, Los Alamos National Laboratory, Los Alamos, NM (1990).

[24] H. M. Rietveld, J. Appl. Cryst. **2**, 65 (1969).
[25] A. W. Sleight and J. F. Weiher, J. Phys. Chem. Solid **33**, 679 (1972).
[26] T. Nakagawa, J. Phys. Soc. Jpn. **24**, 806 (1968).
[27] T. Horikubi and N. Kamegashira, Mater. Chem. Phys. **65**, 316 (2000).
[28] C. Kittel, Introduction to Solid State Physics, 6th ed. (John Wiley & Sons, Inc., New York, 1986), p. 406.
[29] G. H. Jonker and J. H. Van Santen, Physica (Amsterdam) **16**, 337 (1950).